Nonlinear Dynamics **21:** 3–29, 2000.

Cellular Buckling in Long Structures

G. W. HUNT[1], M. A. PELETIER[2], A. R. CHAMPNEYS[3], P. D. WOODS[3], M. AHMER WADEE[1], C. J. BUDD[4], and G. J. LORD[5]
[1]*Department of Mechanical Engineering, University of Bath, Bath BA2 7AY, U.K.*
[2]*Centrum voor Wiskunde en Informatica, Amsterdam, The Netherlands*
[3]*Department of Engineering Mathematics, University of Bristol, Bristol BS8 1TR, U.K.*
[4]*Department of Mathematical Sciences, University of Bath, Bath BA2 7AY, U.K.*
[5]*National Physical Laboratory, Teddington, U.K.*

(Received: 8 September 1998; accepted: 22 June 1999)

Abstract. A long structural system with an unstable (subcritical) post-buckling response that subsequently restabilizes typically deforms in a cellular manner, with localized buckles first forming and then locking up in sequence. As buckling continues over a growing number of cells, the response can be described by a set of lengthening homoclinic connections from the fundamental equilibrium state to itself. In the limit, this leads to a heteroclinic connection from the fundamental unbuckled state to a post-buckled state that is periodic. Under such progressive displacement the load tends to oscillate between two distinct values.

The paper is both a review and a pointer to future research. The response is described via a typical system, a simple but ubiquitous model of a strut on a foundation which includes initially-destabilizing and finally-restabilizing nonlinear terms. A number of different structural forms, including the axially-compressed cylindrical shell, a typical sandwich structure, a model of geological folding and a simple link model are shown to display such behaviour. A mathematical variational argument is outlined for determining the global minimum postbuckling state under controlled end displacement (*rigid* loading). Finally, the paper stresses the practical significance of a Maxwell-load instability criterion for such systems. This criterion, defined under dead loading to be where the pre-buckled and post-buckled state have the same energy, is shown to have significance in the present setting under rigid loading also. Specifically, the Maxwell load is argued to be the limit of minimum energy localized solutions as end-shortening tends to infinity.

Keywords: Nonlinear buckling, localization, homoclinic, heteroclinic, restabilization, Maxwell criterion.

1. Introduction

Subcritical bifurcation in a long structure will often lead to a localized buckle pattern that is usefully described as a homoclinic orbit of a dynamical system in which an infinite spatial co-ordinate x plays the role of time. There has thus been a corresponding flurry of activity in recent years at the interface between mathematics and mechanics, exploring and describing such phenomena (see, for example, [1]). The buckling of cylindrical shells [2] and twisted rods [3, 4] are two important examples now known to display such responses. Although the nonlinear nature of these problems leads to a certain 'spatial chaos' [5], the underlying bifurcation structure of such buckling behaviour is now well understood. Similarly, supercritical bifurcation, which tends to lead to periodic responses, is again reasonably well documented [6].

By comparison however, there has only been a modest level of effort expended on systems that bifurcate in an initially unstable manner but subsequently restabilize. Such behaviour is common to many structural systems; indeed it could be argued that, unless it fractures or oth-

erwise collapses, restabilization is typical of any structure that in the first instance is unstable. The combination calls for an interesting mix of buckling behaviour: the potential to localize is reflected in the existence of homoclinic connections from the unbuckled equilibrium state to itself, yet periodicity, associated with the restabilization, must also play a role. Such issues raise interesting and challenging mathematical questions, some of which are addressed here, others being left for future work.

The paper has three distinct aims. The first, addressed Section 2, is to introduce the phenomena in question via a simple model, which we choose partly for historical reasons to be that of an axially-compressed linear elastic strut undergoing moderately large displacements into a nonlinear Winkler medium. To provide the appropriate response, the foundation itself is given a constitutive relation that first destabilizes and then restabilizes. Energy minimisation then leads to an appropriate fourth-order ordinary differential equation (ODE) for the deflection as a function of a single space variable. The equation includes naturally a parameter that measures the degree of restabilization against that of the initial destabilization. If the parameter is large, restabilization swamps the response and all localized (homoclinic) behaviour is lost. On the other hand if it is small, destabilization holds sway and the response is essentially unchanged from known homoclinic behaviour. Over an intermediate range, however, the response is governed by sets of homoclinic responses of differing lengths that lead in the limit to heteroclinic connection between the unbuckled and periodically-buckled equilibrium states. In so doing the fundamental localized response in load–deflection space oscillates back and forth over a finite range of loads. At each fold in such a curve, the homoclinic mode picks up an additional buckling 'cell'. More details of the numerical and normal-form-analysis techniques used and more extensive numerical results can be found in [7].

Our second intention, fulfilled in Sections 3 and 5, is to demonstrate the wide range of applicability of this cellular buckling mechanism in a number of different structural examples. The mechanism has already been described in a cylinder buckling model in [8] where its connection with the so-called Maxwell-load condition for calculating realistic failure loads is discussed. Here we extend those results for the cylinder and also point to applications arising from our recent studies on a certain sandwich material used in the manufacture of light structures [9, 10] and on models for geological folding [11, 12].

Thirdly, in Section 4 we point to some more mathematically rigorous ideas for proving some of the heuristic arguments underlying our explanations and for deciding which among a sequence of possible numbers of buckled cells may be the minimum energy configuration for a given end-shortening. This leads to the concept of the Maxwell load, which we first explore for a hypothetical link model. These results are generalized for smooth systems and variational arguments are used to show that as end shortening tends to infinity, along the oscillating path described in Section 2, the minimum energy solutions tend to the Maxwell load.

We should point out that many of the techniques of analysis used transcend structural engineering. For example, the mechanism we describe also has potential application in pattern-formation problems (Equation (1) below arises in a generalized Swift-Hohenberg partial differential equation [13]).

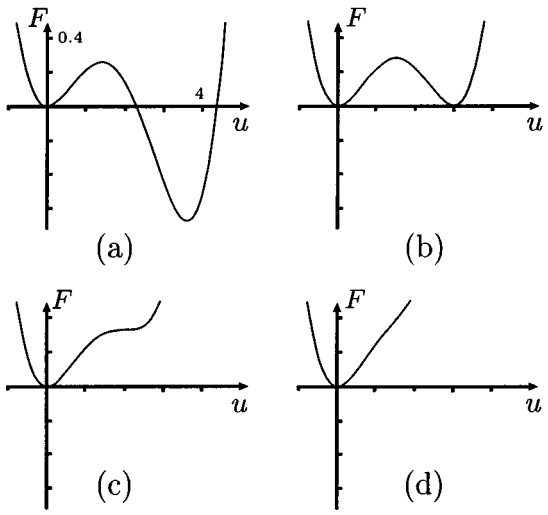

Figure 1. Foundation energy F plotted for $f(u) = f_1(u) = u - u^2 + bu^3$. (a) $b = 0.2$; (b) $b = 2/9$; (c) $b = 1/4$; (d) $b = 0.3$.

2. Strut Model

In this section, we work out in detail the process of buckling applied to the canonical dimensionless model of a strut resting on a nonlinear foundation:

$$u'''' + Pu'' + f(u) = 0, \quad \text{where} \quad \begin{cases} \text{either} \quad f(u) = f_1(u) = u - u^2 + bu^3, \\ \text{or} \quad f(u) = f_2(u) = u - u^3 + \alpha u^5. \end{cases} \tag{1}$$

See [14, 15] and references therein for the assumptions underlying this model, its derivation from energy minimisation and the interpretation of the variables in dimensional versions of this equations. Broadly speaking, u represents the deflection of the strut, primes denote differentiation with respect to a co-ordinate x running along its length, and P is the strength of a compressive load. We are interested in long struts and for that reason assume that $x \in (-\infty, \infty)$. The form of the restoring force $f(u)$ provided by the foundation is taken to model the effect of a restiffening nonlinearity after an initial destiffening of the foundation. The two alternative forms of f describe respectively an asymmetric and symmetric form of foundation, reflecting the difference between a one-sided supported structure and an embedded structure (see Section 3.2 below for some motivation for the latter in structural geology).

For the rest of the present section, we shall consider the asymmetric nonlinearity f_1, where the coefficient $b > 0$ models the degree of restiffening compared with the initial destiffening represented by the u^2 term (whose coefficient has been scaled to unity under non-dimensionalisation). Graphs of the energy stored in the foundation for different values of b are shown in Figure 1.

Let us briefly collect a few facts about Equation (1). First, since it is derived from energy minimisation, it is a conservative system. Moreover, with x playing the role of time, the fourth-order equation may be regarded (under a change of co-ordinates) as two-degree-of-freedom Hamiltonian dynamical system with (constant) Hamiltonian 'energy' given by

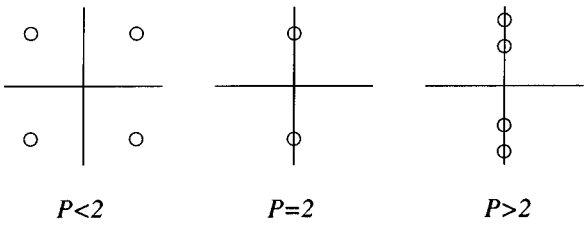

Figure 2. The behaviour of eigenvalues at the Hamiltonian–Hopf bifurcation.

$$H = u'u''' + \frac{P}{2}u'^2 - \frac{1}{2}u''^2 + F(u), \quad \text{where} \quad F(u) = \int_0^u f(v)\,\mathrm{d}v. \tag{2}$$

Second, the dynamical system is also reversible (in the sense of [16]), that is Equation (1) is invariant under

$$R : (u', u''') \to (-u', -u''') \quad \text{and} \quad x \to -x. \tag{3}$$

Finally, note that spatially homogeneous equilibrium configurations are given by the equations,

$$u = 0, \quad 1 - u + bu^2 = 0. \tag{4}$$

so that only the fundamental (unbuckled) flat state at $u = 0$ exists if $b > 1/4$. Linearizing about this trivial equilibrium we find that eigenvalues λ are given by $\lambda^4 + P\lambda^2 + 1 = 0$. Hence for $-2 < P < 2$, we have a complex quadruple of eigenvalues $\pm\mu \pm i\omega$ for some $\mu, \omega > 0$. We call such an equilibrium a *saddle-focus*. Moreover, as P increases through 2 these eigenvalues coalesce at $\pm i$ and become two imaginary pairs. Hence $P = 2$ corresponds to the linear buckling load of the strut and corresponds to a *Hamiltonian-Hopf* bifurcation (see Figure 2).

We are interested in deflections that decay to zero at both ends, i.e. $u \to 0$ as $|x| \to \infty$. These represent homoclinic solutions of the ODE. An important class of homoclinic solutions is formed of those that are symmetric under the reversibility. A neat way of characterizing such trajectories is that they are formed by a point of intersection of the unstable manifold of the origin $W^u(0)$ and the *symmetric section* $\mathcal{S} := \{(u, u', u'', u''') : u' = u''' = 0\}$ of the reversibility. Much is known about homoclinic solutions (symmetric or otherwise) to Equation (1) in the case when $b = 0$ [17]. Here a primary homoclinic solution (localized buckling mode) bifurcates subcritically from $P = 2$ and survives all the way back to $P = -\infty$. For $-2 < P < 2$ there are also infinitely many *N-pulsed* localized solutions (which resemble N copies of the primary placed end to end) for each $N > 2$, that lie on paths that do not bifurcate from zero amplitude.

2.1. Hamiltonian–Hopf Bifurcation: Normal Form and Asymptotics

Let us now consider more closely the behaviour of solutions to Equation (1), with $f = f_1$, by looking at what happens close to the linear buckling condition $P = 2$ through a study of the truncated normal form for *any* dynamical system undergoing a Hamiltonian–Hopf bifurcation. To use this normal form we introduce new complex coordinates A and B which are smooth transformations of the original functions u, u_x, u_{xx} and u_{xxx}. Furthermore, we introduce a new

time variable t which is a smooth transformation of x. In this transformed set of coordinates a homoclinic solution in which $u(x)$ and its derivatives tend to zero as $|x| \to \infty$, transforms to a homoclinic solution in which $|A(t)|$ and $|B(t)|$ both tend to zero as $|t| \to \infty$. Similarly fixed points and periodic solutions in the original variables transform to qualitatively similar solutions. Thus the interesting dynamics of the original problem can be studied by looking at the dynamics of the transformed system without explicitly giving the transformation.

Following [18, 19] the normal form of the Hamiltonian–Hopf bifurcation may be written in the form

$$\frac{\mathrm{d}A}{\mathrm{d}t} = i\omega A + B + iA\,\Phi\left(\mu; |A|^2, \frac{i}{2}(A\bar{B} - \bar{A}B)\right) + R_A, \tag{5}$$

$$\frac{\mathrm{d}B}{\mathrm{d}t} = i\omega B + iB\,\Phi\left(\mu; |A|^2, \frac{i}{2}(A\bar{B} - \bar{A}B)\right) + AQ\left(\mu; |A|^2, \frac{i}{2}(A\bar{B} - \bar{A}B)\right) + R_B. \tag{6}$$

Here Φ and Q are polynomials with real coefficients which to lowest order take the form

$$\Phi(\mu; y, w) = p_1\mu + p_2 y + p_3 w, \quad Q(\mu; y, w) = -q_1\mu + q_2 y + q_3 w + q_4 y^2, \tag{7}$$

and R_A and R_B are terms of higher order. The parameter μ is such that the bifurcation occurs at $\mu = 0$. The truncated system with $R_A = R_B = 0$ is completely integrable with two first integrals

$$K_1 = A\overline{B} - \overline{A}B, \quad K_2 = |B|^2 - \int_0^{|A|^2} Q(\mu, s, i/2K_1)\,\mathrm{d}s.$$

In what follows, the coefficients of Φ are unimportant and q_3 plays a subservient role. Also, without loss of generality, $q_1 > 0$. Then it is only the sign of the coefficient q_2 that is important [19]. However, when q_2 is small, one has to look at the sign of q_4.

For Equation (1), a calculation [7] of the transformation required to obtain the normal form (5), (6) gives

$$\mu = P - 2, \quad q_1 = \frac{1}{4}, \quad q_2 = -\frac{19}{18} + \frac{3}{4}b, \quad q_4 = \frac{12007}{576}b - \frac{687295}{46656} - \frac{327}{512}b^2 \tag{8}$$

and

$$q_3 = \frac{118}{81} - b, \quad p_1 = -\frac{1}{4}, \quad p_2 = -\frac{4}{27}, \quad p_3 = \frac{64}{81}.$$

So q_2 changes sign at $b = 38/27$ and at this value q_4 is positive. Hence the case where q_2 passes through zero with $q_4 > 0$ is of interest, and we shall regard μ and q_2 (equivalently P and b) as independent small parameters unfolding the codimension two point where they are both zero. Note that Dias and Iooss [20] have analysed this transition for $q_4 < 0$ (motivated by interfacial water waves) which leads to entirely different dynamics.

Suppose first that q_2 is not small. Then making the scaling

$$A(t) = \frac{\sqrt{|\mu|}}{2}\tilde{A}(x)\,\mathrm{e}^{i\omega t}, \quad B(t) = \frac{|\mu|}{2}\tilde{A}(x)\,\mathrm{e}^{i\omega t}, \quad x = \sqrt{|\mu|}t, \tag{9}$$

means that the linear dynamics are factored out and the problem is rescaled into the 'slow space' equation

$$\tilde{A}'' = \tilde{A}\left(-q_1\mu + \frac{q_2}{4}|\tilde{A}|^2\right) \tag{10}$$

up to leading order in $\mu < 0$ [20]. Note that this equation is identical (up to a μ-dependent scaling on A and x) with that calculated in [14] using double-scale asymptotic expansions. From the form of (10) one finds the small amplitude subcritical bifurcation of homoclinic orbits from $\mu = 0$ provided the nonlinear coefficient is negative; that is, provided $q_2 < 0$, the condition known as *subcriticality* in [19].

If q_2 is small, Dias and Iooss [20] show that taking

$$q_2 = \varepsilon, \quad \text{and} \quad A = \mathcal{O}(\sqrt{\varepsilon}), \quad B = \mathcal{O}(\varepsilon\sqrt{\varepsilon}), \quad t = \mathcal{O}(\sqrt{\varepsilon}), \quad \mu = \mathcal{O}(\varepsilon^2),$$

$R_A = R_B = 0$, and the form (7), then the ignored terms are of consistently higher order in ϵ. Using the integrals $K_{1,2}$ one can then integrate the problem explicitly to obtain a single equation for $y = |A|^2$:

$$\left(\frac{\mathrm{d}y}{\mathrm{d}t}\right)^2 = 4\left(y\left(K_2 + \int_0^{|a|^2} Q(\mu, s, K_1)\,\mathrm{d}s\right) - K_1^2\right) := 4G(y). \tag{11}$$

This may be interpreted as the equation of a particle with zero total energy that is confined to lie in a well with potential $-4G(y)$. The function G is of the form

$$G(y; \mu, K_1, K_2) = \frac{1}{3}q_4 y^4 + \frac{1}{2}q_2 y^3 - (q_1\mu - q_3 K_1)y^2 + K_2 y - K_1^2. \tag{12}$$

We want to understand solutions which decay to zero as $|t| \to \infty$ and hence we take $K_1 = K_2 = 0$. Thus, dividing out the double root of G at the origin leaves the quadratic

$$g(y) = \frac{q_4}{3}y^2 + \frac{q_2}{2}y - q_1\mu, \tag{13}$$

which has two roots in the case of interest ($q_4, q_1 > 0$, $q_2 < 0$). Figure 3 shows graphs of $G(y)$ as q_2 and μ are varied. From the shape of the graphs we note that in parameter region 2 there are homoclinic orbits to the origin (note that region 5 does not correspond to homoclinic orbits since $y = |A|^2$ must be positive). This region has two boundaries: $\mu = 0$, which is the Hamiltonian Hopf point; and where the discriminant of D_g of $g(y)$ is zero, i.e. $\mu = -(3/16)q_2^2/(q_1 q_4)$. Along the latter, there is a non-trivial double root of f, which corresponds in the full system to a periodic orbit with non-zero amplitude. The shape of f then shows that the homoclinic orbit to the origin has become a heteroclinic connection between the origin and the periodic orbit. This heteroclinic orbit will play a crucial role in the numerical experiments that follow.

2.2. Heteroclinic Tangencies and Numerics

For $q_2 < 0$, after incorporating the phase of the complex variables A and B, for the normal form (5) (but still with $R_A = R_B = 0$) we have the subcritical ($\mu < 0$) bifurcation of a phase-angle parametrized family of homoclinic solutions to a saddle focus at the origin. A calculation in [19] shows that when remainder terms are included that break the completely integrable structure of the normal form, two reversible homoclinic connections persist among this family. In fact, if one could prove that these two orbits are transverse in the sense of [21] (they almost certainly are), then Devaney's construction [22] additionally gives infinitely many N-pulse orbits for each N and each small μ, although none of them bifurcates from $\mu = 0$.

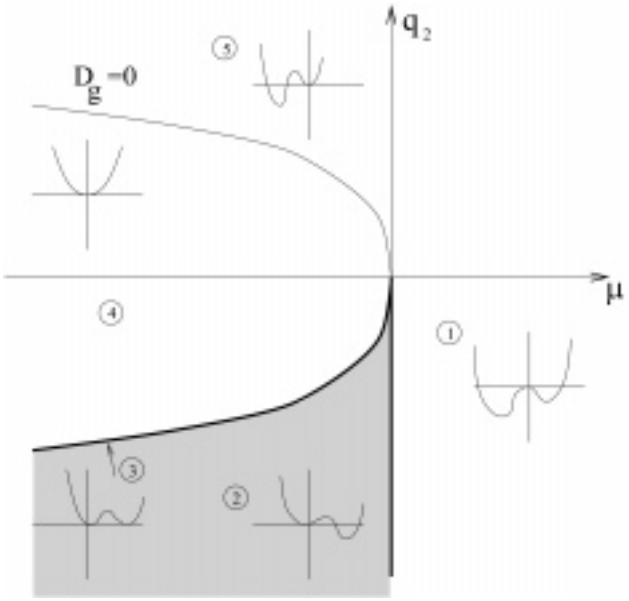

Figure 3. Summary of the behavior for $q_4 > 0$.

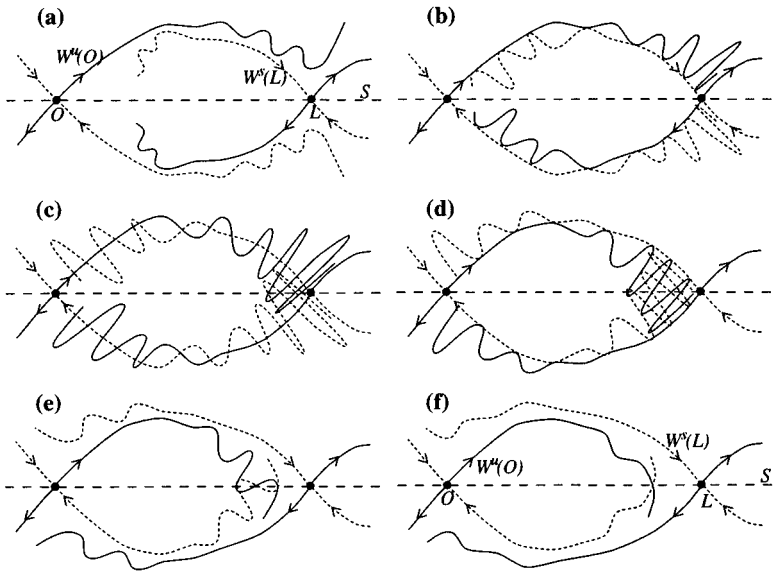

Figure 4. Illustrating the parameter unfolding of two successive heteroclinic tangencies between a saddle-focus equilibrium O and a saddle-type periodic orbit L for a four-dimensional reversible Hamiltonian system. The picture is drawn schematically by taking a formal Poincaré section within the zero level set of the Hamiltonian function, S is the symmetric section, and unstable and stable manifolds are depicted respectively by solid and broken lines. Each point at which $W^u(0)$ intersects S corresponds to a symmetric homoclinic orbit.

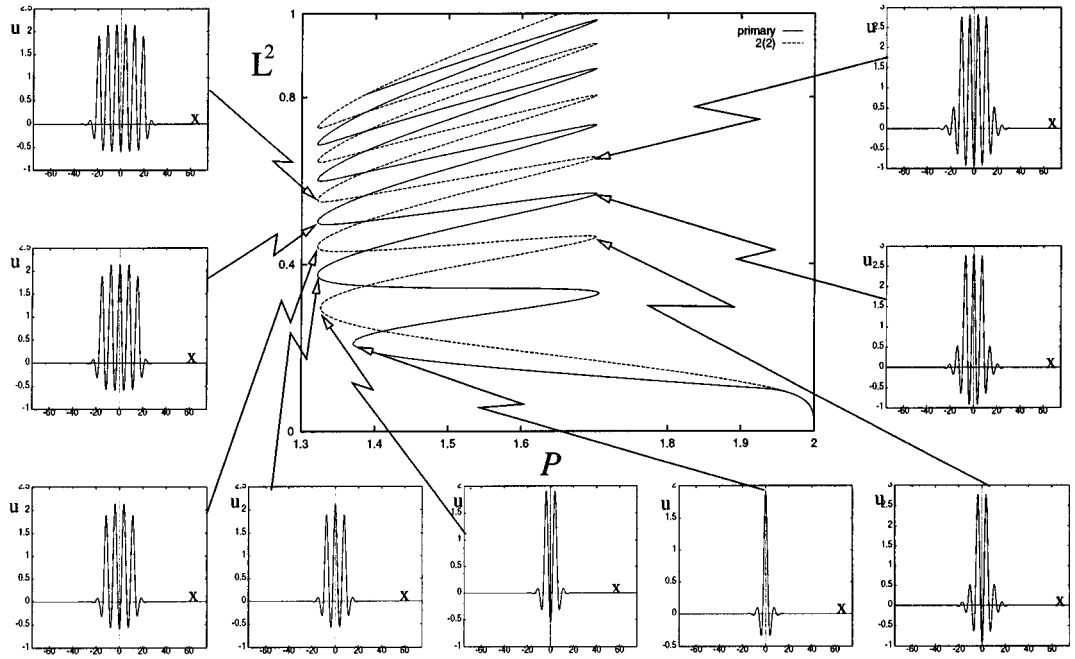

Figure 5. Continuation in P of the primary and **2**(2) homoclinic orbit from the reversible-Hopf bifurcation at $P = 2$ of Equation (1) with $b = 0.29$. These and subsequently presented numerical results were computed using the continuation code AUTO [23]. The L^2-norm represented is a scaling of the vector norm of $(u(x), u'(x), u''(x), u'''(x))$.

Now let us consider what happens to the zero-to-periodic heteroclinic connection, which for the normal form, Equation (5), occurs at an isolated parameter μ-value, $\mu = -(3/16)q_2^2/(q_1 q_4)$, and accounts for the sudden destruction of homoclinic orbits to the origin. When normal-form breaking remainder terms are added, such a heteroclinic connection is structurally unstable and would lead generically to a pair of heteroclinic tangencies occuring at nearby parameter values. Figure 4 shows how such an unfolding leads to a strange bifurcation sequence of homoclinic orbits (intersections between $W^u(0)$ and the *symmetric section* S). This sequence has been computed numerically for the primary homoclinic solutions of (1) as shown in Figure 5. The path corresponds to single curve of homoclinic orbits to the origin undergoing a snaking curve, involving successive folds as the solution generates more and more bumps (oscillations close to the periodic orbit). For a more detailed justification of the construction in Figure 4 and why it leads to such a snaking curve, the reader is referred to [8]. In fact, each of the two homoclinic orbits that bifurcate from $P = 2$ undergoes a snaking sequence as in Figure 5. The linked nature of these two sequences is apparent in Figure 6a. Note that the other branch coming from $P = 2$ may be considered as a 2-pulse orbit (**2**(2) in the notation of [17]).

As b is decreased towards $38/27$, the value at which $q_2 = 0$ for Equation (1), the oscillations in P decrease in amplitude (see Figure 6a). Figure 6b shows the distribution of limit points as μ and q_2 are varied for Equation (1).

Note finally that to prove categorically for Equation (1), that the non-structurally-stable heteroclinic orbit of the normal form breaks up in the way just described, would require a careful Melnikov-type calculation.

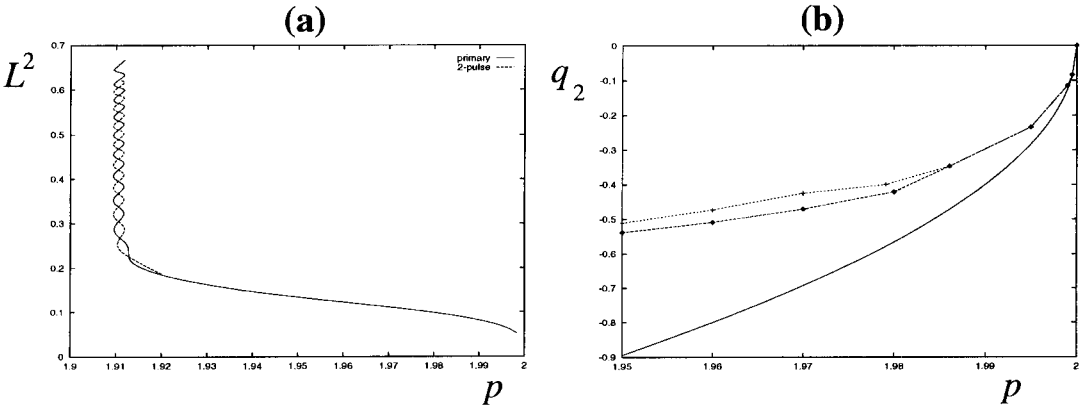

Figure 6. (a) Similar to Figure 5 but for $b = 0.594$. (b) Left and right-hand limit points at the top of the snaking sequence of the primary homoclinic orbit as P and b are varied close to the codimension-two point where $P = 2, q_2 = 0$. The solid line represents the theoretical curve calculated from the normal form, $q_2^2 = 16(2 - P)q_1q_4/3$.

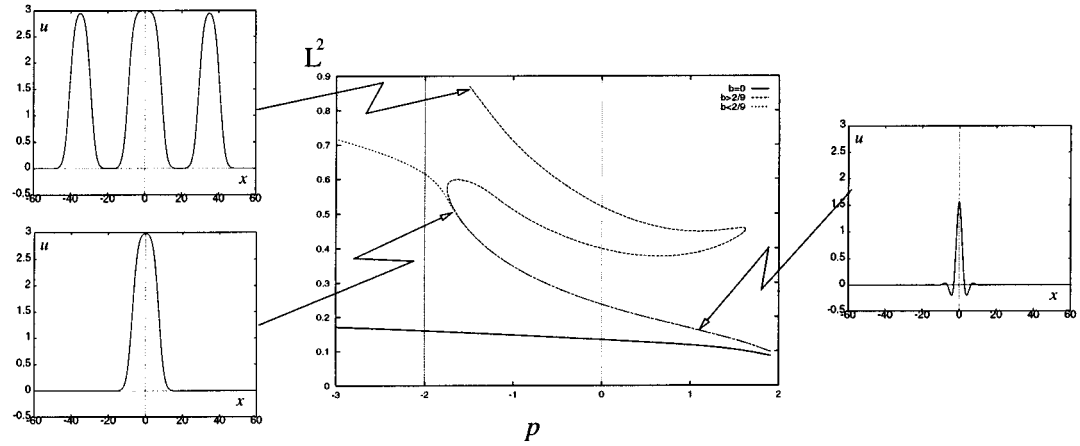

Figure 7. Continuation in P of the primary solution starting at the reversible Hopf for $b = 0$, $b = (2/9)^-$, and $b = (2/9)^+$. The insets show that, as the transition $b = 2/9$ is approached, the orbits on the snaking bifurcation curve approach multi-bump version of a 'kink' connection between $u = 0$ and $u = 3$.

2.3. KINKS – A DEGENERATE BIFURCATION DIAGRAM

For $b = 0$, it is known (at least numerically) that the primary branch born in the reversible-Hopf bifurcation at $P = 2$ can be traced all the way back to $P = -\infty$, including passing through the 'node focus transition' of the origin at $P = -2$ (see [17] and references therein). The transition that must take place between this and large b-values is partially summarized in Figure 7. In fact the transition occurs at precisely $b = 2/9$, at which value there is a non-trivial equilibrium at $u = 3$ that has exactly the same energy (value of the H) as the origin (see Figure 1b). Therefore there is the possibility of heteroclinic connections between $u = 0$ and $u = 3$ (in the parlance of pattern formation, we shall refer to such solutions as *kinks*). This indeed is found numerically to occur, and to account for the end of the snaking curve as indicated in Figure 7.

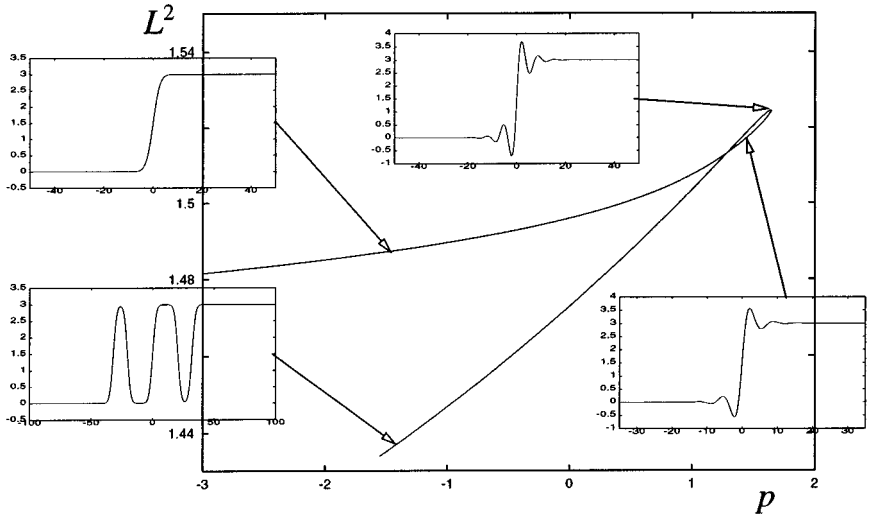

Figure 8. Kink solutions for $b = 2/9$.

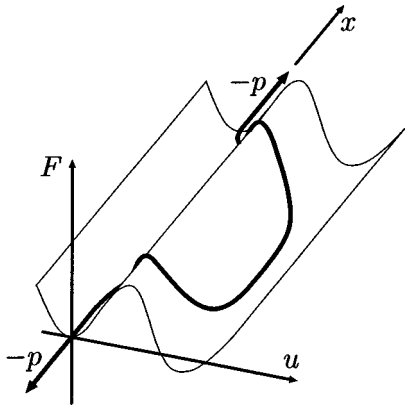

Figure 9. Potential energy surface for the foundation, and flexible rod analogy.

Precisely at the parameter value $b = 2/9$ we have the curve of heteroclinic connections, in P *versus* norm space, represented in Figure 8. The 'primary' kink solution survives all the way back to $P = -\infty$. In fact, at this b-value, the transformation $u \to 2u/3 - 1$ turns Equation (1) with $f = f_1$ into that with $f = f_2$ and $\alpha = 0$. This equation in turn is the steady state equation for the so-called extended Fisher–Kolmogorov equation, the existence of kink solutions for which has been rigourously proved [24–27]. We may also interpret such solutions physically. Figure 9 shows a sketch of energetically how such solutions might arise for the strut model, by plotting the foundation energy F against u and x, for $P < -2$ and $b < 2/9$. The tensile load $-P$ and bending curvature $\mathrm{d}^2u/\mathrm{d}x^2$ both act to pull out the loop of a model heavy flexible rod that hangs over the potential ridge. Note that the rod has no stiffness in the vertical F sense, and similarly vertical differential displacement does not contribute to the work done by the load. To balance these tendencies to straighten, the rod must drop to a value of F that lies below the fundamental minimum at $u = 0$. If the second minimum at $u \neq 0$ is only just below the first, a long length of loop is required, giving a stretched-out

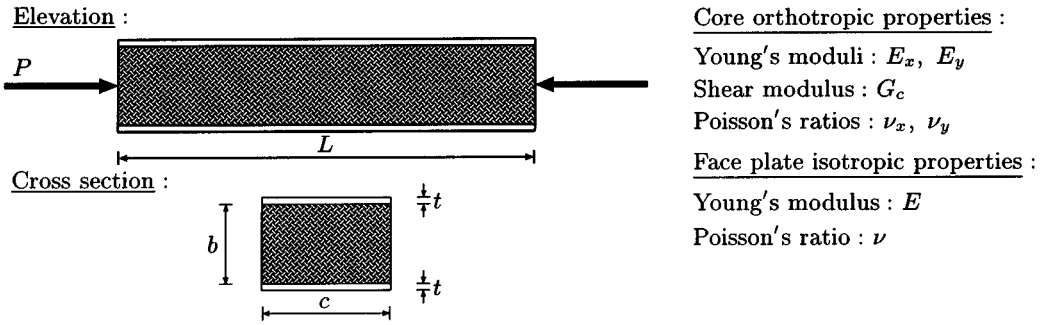

Figure 10. Typical sandwich panel, cross-section and material properties.

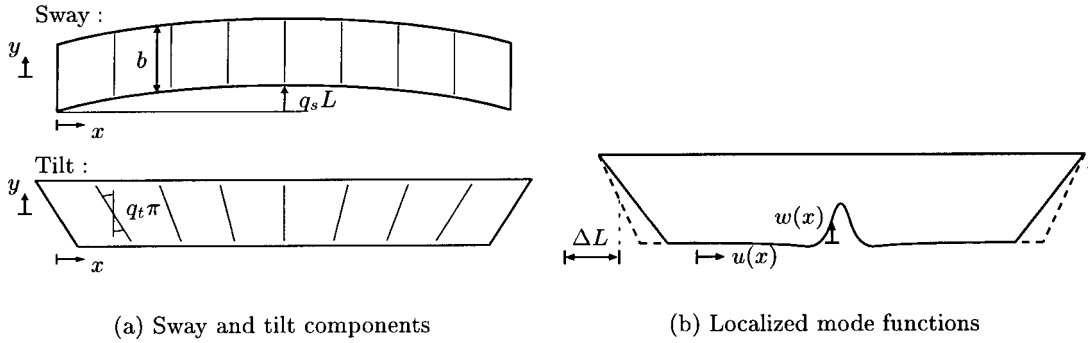

Figure 11. Overall mode and localized mode definitions.

homoclinic form; as $b \to 2/9$ this length must grow to infinity. A mechanism for heteroclinic connection from the flat state at $u = 0$ to periodic states in the range $-2 < P < 2$ is thus born at $b = 2/9$ and $P = -2$.

3. Other Examples

We next turn to two other examples of buckling problems that appear to have the same qualitative features as those just outlined for the simple strut. After a brief discussion of global Maxwell criteria of instability a third important example, the axially-compressed cylindrical shell, is introduced in Section 5 as a final, practically-significant, illustration of the sequential instability mechanism.

3.1. A Sandwich Structure

Figure 10 shows a typical sandwich structure in compression with its geometric and material definitions. The total potential energy of the system, V, is defined below in Equation (14). This is formulated to describe the interactive buckling behaviour of such a structure – the interaction being between an overall, Euler-type, mode and a local mode, which combine to give localized buckling, where the degrees of freedom and the functions for the equations are defined in Figure 11. Applying the calculus of variations on V, we can derive differential equations for w and u; minimizing V with respect to the degrees of freedom q_s, q_t, and Δ, we obtain integral constraints all of which are detailed in recent papers [9, 10]. The structure tends

to buckle in an overall mode first; this puts the faces under differing amounts of compression: the functions $w(x)$ and $u(x)$ define the deflection of the face under greater compression once the overall mode grows enough to induce localized buckling.

$$
\begin{aligned}
V \;=\; \int_0^L \Bigg\{ & C_x \left[\Delta^2 + q_t^2 \frac{b^2\pi^4}{12L^2} \sin^2 \frac{\pi x}{L} + \frac{1}{3}\dot{u}^2 + \frac{1}{20}\dot{w}^4 \right. \\
& \left. - \Delta\dot{u} - \frac{1}{3}\Delta\dot{w}^2 - q_t \frac{b\pi^2}{6L} \sin \frac{\pi x}{L} \left(\dot{u} + \frac{1}{2}\dot{w}^2 \right) + \frac{1}{4}\dot{u}\dot{w}^2 \right] \\
& + \frac{1}{2}kw^2 - \frac{1}{3}k_1 w^3 + \frac{1}{4}k_2 w^4 + G \left[\frac{u^2}{b^2} - \frac{u\dot{w}}{b} + \frac{1}{3}\dot{w}^2 + (q_s - q_t)^2\pi^2 \cos^2 \frac{\pi x}{L} \right. \\
& \left. + (q_s - q_t)\pi \cos \frac{\pi x}{L} \left(\dot{w} - \frac{2}{b}u \right) \right] \\
& + C_y \left[\nu_x^2 \Delta b \left(\dot{u} - \Delta + \frac{1}{3}\dot{w}^2 \right) - \nu_x \left(\dot{u}w + \frac{1}{3}w\dot{w}^2 \right) \right] \\
& + D \left[2\Delta^2 + \frac{1}{4}\dot{w}^4 - \left(2\Delta + q_t \frac{b\pi^2}{L} \sin \frac{\pi x}{L} \right) \left(\dot{u} + \frac{1}{2}\dot{w}^2 \right) \right. \\
& \left. + q_t^2 \frac{b^2\pi^4}{2L^2} \sin^2 \frac{\pi x}{L} + \dot{u}^2 + \dot{u}\dot{w}^2 \right] \\
& + \frac{1}{2}EI \left(\ddot{w}^2 + 2q_s^2 \frac{\pi^4}{L^2} \sin^2 \frac{\pi x}{L} \right) - P \left(\frac{q_s^2\pi^2}{2} \cos^2 \frac{\pi x}{L} - \frac{1}{2}\dot{u} + \Delta \right) \Bigg\} \, \mathrm{d}x. \qquad (14)
\end{aligned}
$$

Material properties are encompassed in the following definitions, including the critical load, P^{C}:

$$
\begin{aligned}
EI \;&=\; \frac{Ect^3}{12(1-\nu^2)}, \quad D = \frac{Etc}{2}, \quad G = \frac{G_c cb}{2}, \quad C_x = \frac{E_x bc}{2(1-\nu_x\nu_y)}, \\
C_y \;&=\; \frac{E_y c}{2(1-\nu_x\nu_y)}, \quad k = \frac{E_y c}{(1-\nu_x\nu_y)b}, \\
P^{\mathrm{C}} \;&=\; \frac{2\pi^2 EI}{L^2} + \frac{2G}{1+s}, \quad s = \frac{2GL^2}{b^2\pi^2} \left(D + \frac{C_x}{6} \right)^{-1}. \qquad (15)
\end{aligned}
$$

The restabilizing aspect in this structure comes into the behaviour of the core; this is usually made of two or three-dimensional cellular materials such as polystyrene or polyurethane foams. In compression, these materials tend to behave with an initially positive stiffness (k), destabilizing to zero or slightly negative stiffness when the microscopic cells in the core material buckle elastically (fall in stiffness represented by $k_1 > 0$), and finally restabilizing when the adjacent cells collapse and bear against each other (rise in stiffness represented by $k_2 > 0$) [28, 29]. This destabilization–restabilization is modelled by a cubic approximation, as in Equation (1) with $f = f_1$. We present numerically obtained solutions to the equations derived from V for an aluminium faced panel: $E = 69$ kN/mm^2, $\nu = 0.3$, $t = 0.5$ mm, $b = 50$ mm, $L = 500$ mm, $c = 250$ mm; and an orthotropic foam core with the following

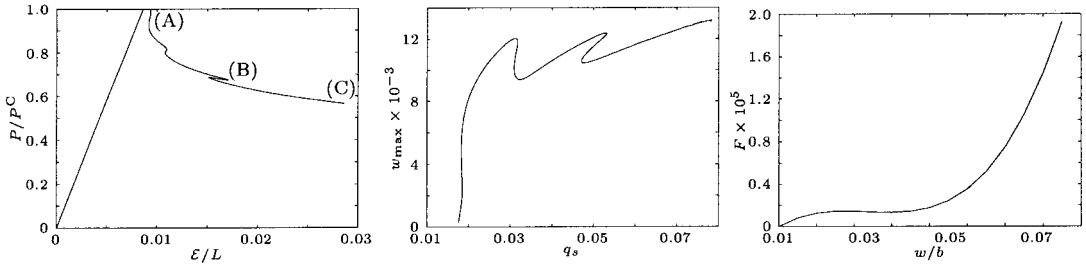

(a) P vs end-displacement

(b) Modal amplitudes of localized and overall buckling

(c) Nonlinear transverse core resistance

Figure 12. Post-buckling response of restabilizing sandwich panel.

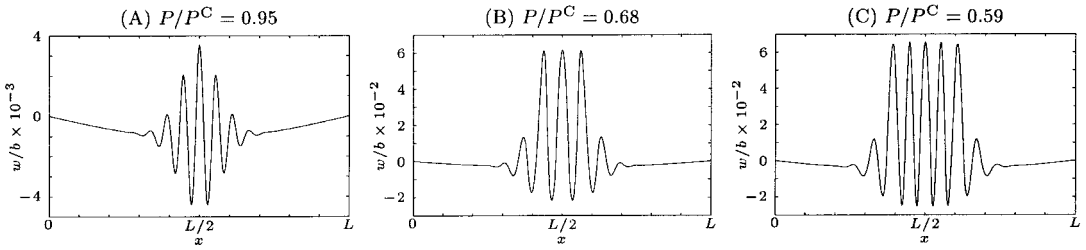

Figure 13. Localized mode profiles of restabilizing sandwich panel. Labels (A), (B) and (C) represent where these occur on the post-buckling path of Figure 12a.

properties: $E_x = E_y = 100$ N/mm^2, $\nu_x = \nu_y = 0.2$ and $G_c = 20$ N/mm^2; with the nonlinearities: $k_1 = 471$ N/mm^3 and $k_2 = 132$ N/mm^4.

Figure 12a shows the characteristic degenerating slope of the post-buckling response; here however the sequential snap-back and restabilization are less obvious than in Figure 5, as the overall load P is affected by a contribution from the unbuckled face. Figure 12b shows the relative amplitude of the localized mode increasing and then decreasing in sympathy with the snapping phenomenon. As the overall mode grows, the single humped solution is transformed into three humps and then five humps and so on, as shown in Figure 13; as in Figure 5, double and four humps do not appear because of prescribed symmetry. Figure 12c shows the chosen core constitutive relation; there is a relatively flat zone before the cubic term begins to take over in the restabilizing region.

3.2. A Model for Geological Folding

Layered rock structures develop an intriguingly wide array of folded patterns. Extensive efforts have been spent in trying to understand the processes responsible for this variety; however, up to the present day, the most successful models have been simple ones that give modest insight into a specific situation. We refer the reader to [30, chapters 10–15] for a discussion of various models and experiments.

One of such simple models is the strut on a foundation, Equation (1), which is often used as a caricature for the folding process in the case of thin layers of rock embedded in thicker layers. Here, both the strut and the foundation are assumed to be elastic; other possibilities are an elastic strut on a viscous foundation [11, 12] or a viscous strut on a viscous foundation [31].

One of the main driving forces in the folding of geological layers is the movement of tectonic plates: where two plates collide, the crustal material at the boundary is gradually squashed and folded. With this in mind the folding is modelled as a prescribed end-shortening process, where the strut buckles as a consequence of the shortening; as time evolves, the shortening increases, and consequently the profile of the buckled strut evolves.

Equation (1) can be obtained as the Euler–Lagrange equation of a variational problem that is inspired by this process. If we introduce the 'strain energy'

$$W(u) = \frac{1}{2}\int u''^2 + \int F(u),$$

and the 'end-shortening'

$$\mathcal{E}(u) = \frac{1}{2}\int u'^2,$$

then we seek the profile u that minimizes the strain energy W under the condition that it has the appropriate amount of end-shortening $\mathcal{E}$; i.e. we seek to solve the variational problem

$$\min_{\mathcal{E}(u)=\lambda} W(u). \tag{16}$$

If a profile u solves this problem, then there exists a Lagrange multiplier P such that

$$W'(u) = P\mathcal{E}'(u), \tag{17}$$

where we write primes for gradients in function space. This equation is in fact identical to Equation (1). This loading condition, where the end-shortening is controlled and the load is a derived quantity, is referred to as 'rigid loading': this can be contrasted with 'dead loading', where the load is controlled without regard to the end-shortening.

We can now create an 'evolution' by varying the end-shortening λ and observing the ensuing profiles. Since the situation is simpler for the nonlinearity f_2 than for f_1 (because of the additional symmetry $u \mapsto -u$ present in f_2) we choose $f = f_2$ for the extent of this section.[1] Note that the destiffening-restiffening property of f implies that

1. for small $s > 0$, the measure of stiffness, $f(s)/s$, decreases as s increases;
2. for larger s, $f(s)/s$ increases again.

This has consequences for the 'evolution' obtained by varying λ in Equation (16):

1. For small λ, minimizers of Equation (16) are small in amplitude, and therefore $f(s)/s$ is decreasing in s over the range of u. This leads to localized profiles.
2. As λ increases, the amplitude of the profiles increases, and attains values for which $f(s)/s$ is increasing in s.

In preliminary numerical experiments it is observed that when the 'evolution' enters into this second phase, the amplitude grows to a limit, and further increases in λ are followed by a widening of the profile. A roughly periodic section arises, flanked by exponentially decaying tails, and a further increase in λ causes the number of oscillations in the periodic section to increase.

[1] The choice of this particular function for the stress-strain relationship of a foundation composed of rock is not as far-fetched as it may seem. The geometry of a deformed layer introduces nonlinearities that Equation (1) does not take into account; these have a destiffening effect [32]. For larger deformations a geometrically nonlinear elastic foundation will show a locking-up behaviour that can be interpreted as a restiffening effect. A nonlinearity of type f_2 is a way of introducing these two qualities in the much simpler Equation (1).

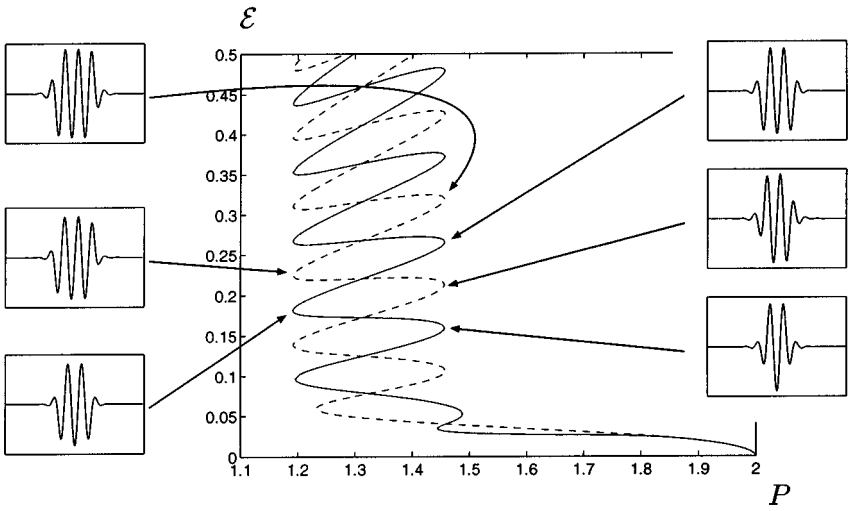

Figure 14. The bifurcation diagram of the homoclinic starting at $P = 2$, for nonlinearity $f(u) = u - u^3 + 3/10\,u^5$.

There is a strong resemblance between this evolution and the form of the solutions that are found along the bifurcation diagram uncovered in Section 2, for example Figure 5. In Figure 14 we draw a bifurcation diagram for the nonlinearity f_2. Although the two figures are similar in appearance, there is a significant difference. In Figure 5 both solution curves consist of *even* solutions; for the nonlinearity f_2, with the additional symmetry $u \mapsto -u$, these two sets of solutions are identical (up to a reflection $u \mapsto -u$) and we draw them as one curve in Figure 14 (continuous line). Because of the additional symmetry, there is also a new reversibility in the problem:

$$\overline{R} : (u, u'') \to (-u, -u'') \quad \text{and} \quad x \to -x,$$

(compare with Equation (3)). This leads to a second curve of solutions, bifurcating from $P = 2$, which are *odd* (broken line). Further numerical results have found that the bifurcation sequence for f_2 is the qualitatively similar to that for f_1 with the equivalent of the kink transition at $b = 2/9$ corresponding to $\alpha = 3/16$. The degenerate Hamiltonian Hopf which occurs for f_1 at $b = 38/27$ has no analogue for f_2 other than formally as $\alpha \to \infty$.

We believe (but have as yet no proof) that the minimizers of Equation (16) all lie on the bifurcation diagram in Figure 14. Every horizontal line in this figure intersects the diagram at least twice, and for large values of λ, by the sloping nature of the curves, more than twice. The oscillations in the graph appear to be centred about a mean value P which is close to the Maxwell load which will be described and computed in the next section. At every value of λ there are therefore several candidates for the global minimizer. In the following section we first explore global minimization issues via a simplified caricature, before investigating more closely the global minimizer for the strut model and its relation to the above diagram.

4. Maxwell Criterion and Global Stability

Let us now turn to the question of which solutions under conditions of controlled end-shortening may be stable. For an environment rich with underlying disturbance, interest

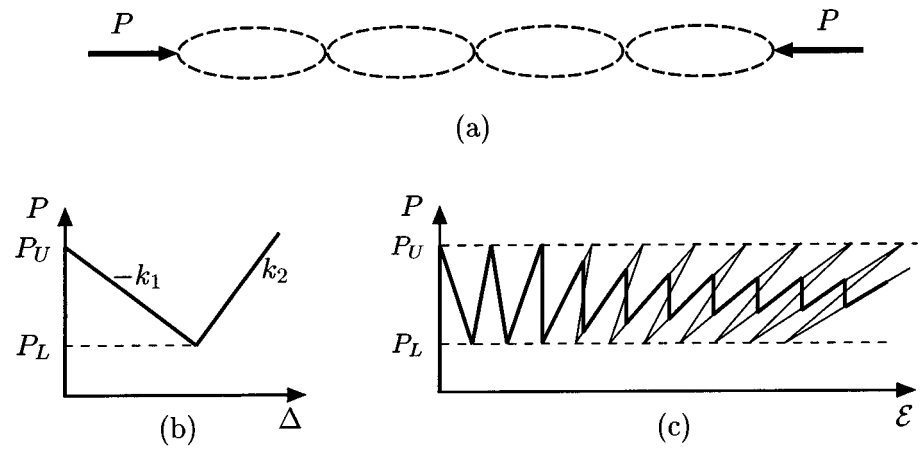

Figure 15. (a) Anti-integrable chain of linked elements. (b) Tri-linear response characteristic for single element, involving regimes of infinite stiffness, negative stiffness, and restabilized positive stiffness. (c) Combined responses.

naturally focuses on the global energy minimum to define the most likely equilibrium configuration. The so-called *Maxwell criterion*, familiar from work on phase transitions (see, for example, [33, p. 53]) is then the controlling mechanism. The following model defines a limiting situation which suggests that the classical *Maxwell load*, where under dead loading conditions the global minimum switches from the pre-buckled to the post-buckled state, holds considerable significance for rigid loading also. Returning to the strut model, it is then demonstrated that the so-called 'zero-energy' periodic solution [34], which matches stored energy with the pre-buckled state and sits at the Maxwell load, is the limit of global minimizers for the homoclinic solutions as end-shortening approaches infinity.

4.1. Physical Interpretation: A Simple Link Model

Consider the anti-integrable chain of linked but uncoupled elements shown schematically in Figure 15a. Individual elements are considered as black boxes each with the response of Figure 15b. In the chain all elements carry the same load P, but deflection in one has no effect on, nor is it affected by, the others. Adding stiffnesses according to a reciprocal law, the combined stiffness on a rising path, R_m, when m individual elements are at stiffness k_2, is given by

$$\frac{1}{R_m} = \frac{m}{k_2} \tag{18}$$

and that of a falling path, F_m, when m elements are at stiffness k_2 but one is unloading at stiffness $-k_1$, is given by

$$\frac{1}{F_m} = \frac{m}{k_2} - \frac{1}{k_1} = \frac{1}{R_m} - \frac{1}{k_1}. \tag{19}$$

Elements are assumed to trigger one-by-one in a random order determined by small imperfections, giving the fanning sequence of equilibrium states shown as light lines in Figure 15c, in which the load oscillates between the upper and lower loads, P_U and P_L, that characterize the response of a single element.

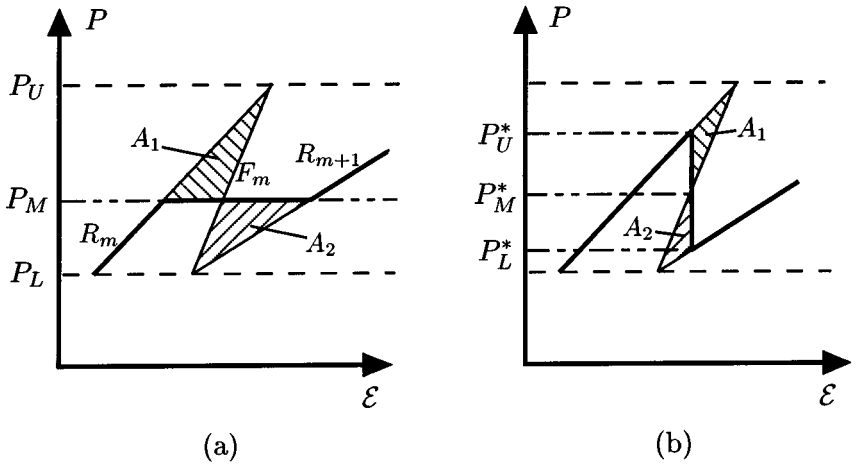

Figure 16. Maxwell criterion in (a) dead loading; (b) rigid loading. For each, $A_1 = A_2$ signals a change in global energy minimum from one rising path to the other.

A general position in the fan is shown in Figure 16. Under conditions of dead loading (Figure 16a), at load P_M the energy hump to be overcome to initiate the next instability is given by area A_1, whereas A_2 represents potentially a release in energy, as in this range the load is greater than that necessary to retain equilibrium. The classical Maxwell load P_M is defined as the load at which the global energy minimum swaps from one equilibrium state to the other – when $A_1 = A_2$ and energy levels on the two rising paths are the same. Simple geometry shows that

$$\begin{aligned} A_1 &= \frac{1}{2}\left(\frac{1}{R_m} - \frac{1}{F_m}\right)(P_U - P_M)^2 = \frac{1}{2}\left(\frac{1}{k_1}\right)(P_U - P_M)^2, \\ A_2 &= \frac{1}{2}\left(\frac{1}{R_{m+1}} - \frac{1}{F_m}\right)(P_M - P_L)^2 = \frac{1}{2}\left(\frac{1}{k_1} + \frac{1}{k_2}\right)(P_M - P_L)^2. \end{aligned} \tag{20}$$

$A_1 = A_2$ then gives,

$$\frac{P_U - P_M}{P_M - P_L} = \sqrt{1 + \frac{k_1}{k_2}}. \tag{21}$$

A_1, A_2 and P_M are all seen to be independent of m, so under dead loading and the necessary disturbance conditions, the Maxwell load P_M signifies the limit of load carrying capacity. Once one element fails they all will fail, albeit in random sequence.

Under rigid loading conditions, transfer takes place when $A_1 = A_2$ of Figure 16b, as the global minimum switches from load P_U^* on the upper to P_L^* on the lower equilibrium state. Simple geometry now gives,

$$\begin{aligned} P_U^* - P_M^* &= \frac{F_m - R_m}{F_m}\left(P_U - P_M^*\right) = \frac{k_2}{mk_1}\left(P_U - P_M^*\right), \\ P_M^* - P_L^* &= \frac{F_m - R_{m+1}}{F_m}\left(P_M^* - P_L\right) = \frac{(k_1 + k_2)}{k_1\,(m+1)}\left(P_M^* - P_L\right), \end{aligned}$$

$$A_1 = \frac{1}{2}\left(\frac{F_m - R_m}{F_m^2}\right)\left(P_U - P_M^*\right)^2 = \frac{1}{2}\left(\frac{mk_1 - k_2}{mk_1^2}\right)\left(P_U - P_M^*\right)^2,$$

$$A_2 = \frac{1}{2}\left(\frac{F_m - R_{m+1}}{F_m^2}\right)\left(P_M^* - P_L\right)^2 = \frac{1}{2}\left(\frac{(k_1 + k_2)\,(mk_1 - k_2)}{(m+1)\,k_1^2 k_2}\right)\left(P_M^* - P_L\right)^2. \qquad (22)$$

$A_1 = A_2$ now gives

$$\frac{P_U - P_M^*}{P_M^* - P_L} = \sqrt{\frac{m}{m+1}\left(1 + \frac{k_1}{k_2}\right)}, \qquad (23)$$

and P_M^*, P_U^* and P_L^* all depend on m. However, comparison with the equivalent form for dead loading (21), shows that as $m \to \infty$, $P_M^* \to P_M$. From the expressions for $P_U^* - P_M^*$ and $P_M^* - P_L^*$ above, it is clear that P_U^* and P_L^* also both approach P_M as $m \to \infty$. This expected form of response under rigid loading is shown as thick lines in Figure 15c. Under rigid loading conditions, as the number of cells increases, all instability accumulates onto the Maxwell load.

4.2. The Maxwell Load for General Systems

Imagine the chain of the previous section encapsulated in a black box. We can apply a load and measure the response in the form of the total shortening of the chain. Under dead-load conditions the response may be very simply described by

1. no response (no shortening) if P is small
2. as P passes a critical value, the system suddenly adopts a large deflection.

The word 'suddenly' is used advisedly – the large-deflection response does not appear smoothly, via smaller deflections, but in the form of a jump. With enough external disturbance, the critical value of the load is P_M, the Maxwell load under dead-load conditions. If the 'large deflection' is interpreted as a failure, then P_M is the limit of load-carrying capacity.

This point of view allows us to generalize the concept of Maxwell load to general extended systems. The response of the strut-on-foundation model under a dead load P is obtained by minimizing the Lagrangian (or total potential energy [35, p. 50])

$$L(u) := W(u) - P\mathcal{E}(u).$$

Here W and $\mathcal{E}$ are the same as in Section 3.2, representing the strain energy and the end-shortening. The second term in L is the work done by the load in shortening the strut. We recall that Equation (1) can be written as $W'(u) - P\mathcal{E}'(u)$, so that a stationary point of L is also a solution of Equation (1).

When P is small, the Lagrangian $L(u)$ is non-negative for any u. Therefore the trivial response, $u \equiv 0$, is the global minimizer. When P passes a threshold value there will be profiles with a negative Lagrangian, so that the zero response is no longer optimal and minimum energy is achieved in a non-zero response. We define the Maxwell load for this system to be this threshold value of P, i.e., P_M is the lowest value of P for which there exist u with $L(u) < 0$. A different way of writing this definition is

$$P_M := \min_{u \neq 0} \frac{W(u)}{\mathcal{E}(u)}, \qquad (24)$$

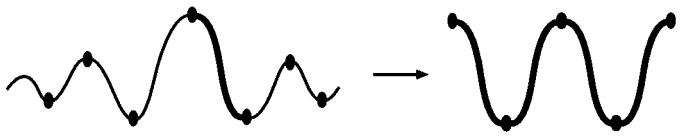

Figure 17. A section between two stationary points is replicated.

where the minimum is taken over all functions for which the integrals in W and $\mathcal{E}$ have meaning.

Let us now consider definition (24) from a different point of view. Suppose that u is a *periodic* function that minimizes the ratio of strain energy to end-shortening, $W(u)/\mathcal{E}(u)$, where the integrals are taken over a period. (Below we shall show that the restriction to periodic functions is natural – that every minimizer of this ratio must, in fact, be periodic.) Taking the gradient of this ratio, we find

$$0 = \left(\frac{W(u)}{\mathcal{E}(u)}\right)' = \frac{1}{\mathcal{E}(u)^2}(\mathcal{E}(u)W'(u) - W(u)\mathcal{E}'(u))$$

which implies that

$$W'(u) = \frac{W(u)}{\mathcal{E}(u)}\,\mathcal{E}'(u).$$

So by comparing this to Equation (17) we find that u solves Equation (1), and in addition we know that

$$P = \frac{W(u)}{\mathcal{E}(u)}. \tag{25}$$

This is equivalent to the statement $L(u) = 0$.

Combining the argument above with definition (24) we find that the Maxwell load P_M reunites a number of interesting features:

1. P_M is the lowest load that produces a non-trivial response;
2. P_M is *numerically equal* to the lowest possible ratio of strain energy to end-shortening, $W/\mathcal{E}$;
3. There exists a periodic function that achieves this minimal ratio, that satisfies Equation (1) for the load $P = P_M$, and has $L = 0$.

We still need to argue why a minimizer of the ratio $W/\mathcal{E}$ is necessarily periodic. Suppose that a function u minimizes the ratio, and that u tends to zero at $\pm\infty$. We will show that we can construct from the function u a periodic function $\tilde{u}$ with a better ratio $W/\mathcal{E}$.

We divide the real line into segments $[x_i, x_{i+1})$, where the x_i are stationary points of u, and compare the value of the ratio $W/\mathcal{E}$ when calculated over such segments instead of over $\mathbb{R}$. It is to be expected that the ratio is not the same for all segments; some segments will have a ratio higher than $W/\mathcal{E}$ calculated over the whole of $\mathbb{R}$, and some a lower ratio. Taking a section with a lower ratio, we construct a periodic function $\tilde{u}$ by gluing segments together, as in Figure 17. The periodic function $\tilde{u}$ then satisfies, by construction, $W(\tilde{u})/\mathcal{E}(\tilde{u}) < W(u)/\mathcal{E}(u)$. This shows that a minimizer of the ratio necessarily is periodic.

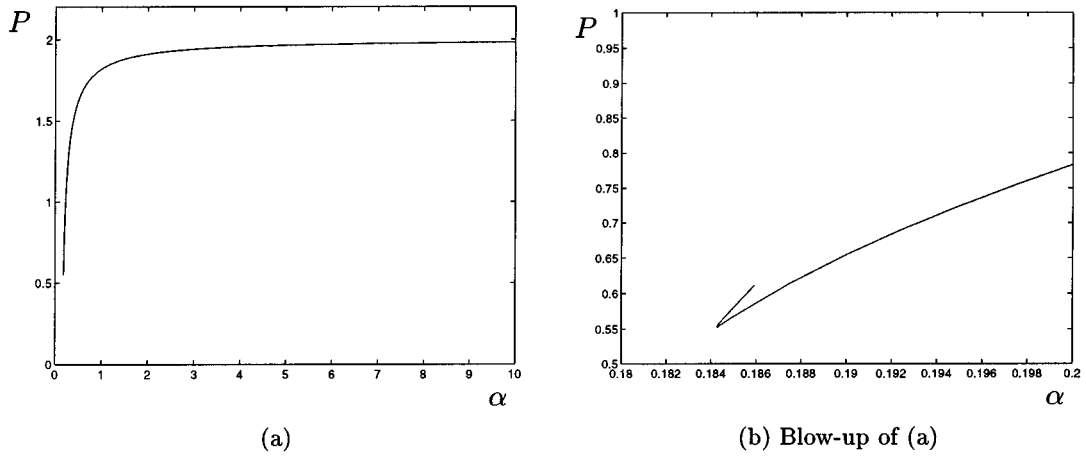

Figure 18. The Maxwell load as a function of α (see the text for details).

We have shown above that the Maxwell load is associated with a periodic solution of Equation (1) that satisfies $L = 0$. Since this solution is found by minimizing a functional over all periodic functions, the period is a free parameter in this minimization. This freedom implies that in addition to $L = 0$, the minimizer has a zero Hamiltonian: this follows by scaling the period and minimizing the ratio with respect to this scaling. We can now calculate the Maxwell load numerically by seeking a periodic solution satisfying $L = H = 0$; see Figure 18, for $f(u) = f_2 = u - u^3 + \alpha u^5$. For this nonlinearity, it is easy to show that $\alpha = 3/16$ is a critical value where the non-zero fixed points $|u| = 2$ solving $f(u) = 0$ have zero Hamiltonian and can thus be a limit points of a heteroclinic connection with the origin . The graph of the Maxwell load extends just below this value before turning back with a rapid increase in the period of the solution as it approaches $3/16$ from below. For large values of α we have that $P \to 2$ and we can show further that the amplitude of the periodic solution in this limit is proportional to $1/\sqrt{\alpha}$.

4.3. The Role of the Maxwell Load under Rigid Loading Conditions

Section 4.1 emphasizes the importance of the Maxwell criterion, not just under the dead loading conditions for which it has been introduced. In the previous section we defined the Maxwell load for a general system under dead loading; here we will show that, as in the case of the chain, the Maxwell load also has a role to play in the behaviour of the system under rigid load.

The thin line in Figure 19 is an impression of the continuous line in Figure 14 (the dashed line corresponds to odd solutions, which we do not consider at this point). The figure shows as thick lines the global minimizer under evolving end shortening. This illustrates the route taken by the system if buckling occurs at the point where energy stored in the foundation is sufficient in magnitude to provoke an instability; an energy hump might remain to be negotiated, but background disturbance is taken to be enough to initiate the jump once the energy level in the post-buckled position is less than that in the pre-buckled state. The system thus always tracks the global energy minimum.

With the anti-integrable chain in mind, we recognize the way the sloping of the curls in this figure reduces the height of the jumps as $\mathcal{E}$ becomes large. Thus we postulate the conjecture

Figure 19. The global minimizers are indicated by the thick lines.

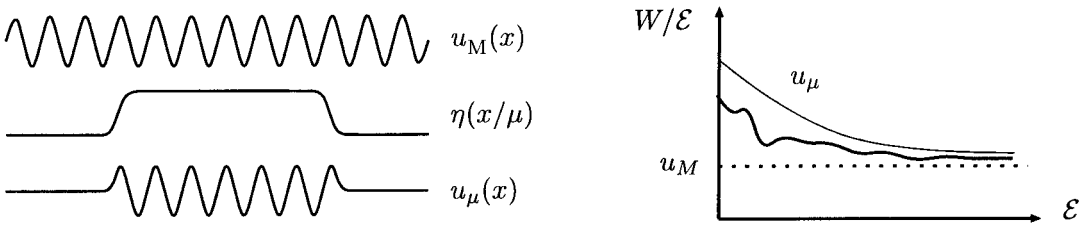

(a) u_μ is a widening section of the minimal periodic function u_{M}

(b) The thick line is the ratio of $W/\mathcal{E}$ for the solution of (16) (schematically)

Figure 20. u_μ provides an upper bound for the ratio $W/\mathcal{E}$ of the solution of Equation (16).

As $\mathcal{E} \to \infty$ the load P of the global minimizers converges to the Maxwell load P_M.

In the previous section it was shown that the Maxwell load under dead-loading conditions (P_M) is associated with the periodic minimizer of the ratio $W/\mathcal{E}$. The relevance of the ratio $W/\mathcal{E}$ to problem (16) becomes apparent when we note that as $\mathcal{E} \to \infty$, solutions of Equation (16) minimize this ratio. This can be recognized by taking the periodic function u_{M} that minimizes the ratio, and defining a sequence of functions

$$u_\mu(x) = \eta(x/\mu)u_{\mathrm{M}}(x),$$

where η is a fixed cut-off function with $\eta \equiv 1$ on $[-1, 1]$ and $\eta \equiv 0$ on $(-\infty, -2] \cup [2, \infty)$. These functions u_μ are shown in Figure 20a. For any given λ we can choose a μ such that $\mathcal{E}(u_\mu) = \lambda$; clearly the minimizer z of (16) then satisfies $W(z) \leq W(u_\mu)$, and $W(u_\mu)/\mathcal{E}(u_\mu)$ is an upper bound for the constrained minimum ratio at $\mathcal{E}(z) = \lambda$. It is directly calculated that $W(u_\mu)/\mathcal{E}(u_\mu)$ converges to the global minimum ratio $W(u_{\mathrm{M}})/\mathcal{E}(u_{\mathrm{M}})$ as $\mu \to \infty$. Therefore the solutions of Equation (16) must also converge to that minimum as $\lambda \to \infty$.

We have shown in the previous section that a minimizer of the ratio $W/\mathcal{E}$ is necessarily periodic (in fact the minimizer is unique). The fact that in the limit $\lambda \to \infty$, the solutions of problem (16) achieve the minimum of the ratio therefore suggests that the profile must come to resemble this periodic solution strongly. The mechanism for doing so is immediate from Figure 14: as the value of $\mathcal{E}$ increases, the solutions spawn additional oscillations, giving rise

to a long periodic section flanked by two tails. This periodic section is in the limit exactly the minimal periodic solution u_{M}.

5. Cylindrical Shell Buckling

Buckling of a long thin axially loaded cylindrical shell is an archetypical example of a long structure which exhibits an unstable response that then restabilizes. We examine that response here in the context of cellular buckling and the Maxwell load. A classical formulation for a thin cylindrical shell of radius r and thickness t is given by the von Kármán–Donnell equations:

$$\begin{aligned} \kappa^2\nabla^4 w + \lambda w_{xx} - \rho\phi_{xx} &= w_{xx}\phi_{yy} + w_{yy}\phi_{xx} - 2w_{xy}\phi_{xy}, \\ \nabla^4\phi + \rho w_{xx} &= \left(w_{xy}\right)^2 - w_{xx}w_{yy}, \end{aligned} \tag{26}$$

where ∇^4 is the two-dimensional bi-harmonic operator, $x \in \mathbb{R}$ is the axial and $y \in [0, 2\pi r)$ is the circumferential coordinate, w is the outward radial displacement measured from an unbuckled state, and ϕ is a stress function [36]. Parameters appearing in Equation (26) are the curvature, $\rho = 1/r$, the geometric constant, $\kappa^2 = t^2/12(1-\nu^2)$, where ν is Poisson's ratio, and loading parameter λ. The parameter λ here plays the role of P in the preceding sections. These equations are derived form the minimization of an energy functional V comprising bending and membrane stretching energy and work done by the load λ.

We discretize the von Kármán–Donnell equations (26) in such a way as to exploit natural symmetries in the problem. Experimentally a well defined number, s, of periodic waves is observed circumferentially [36, 37] in the buckled deformation, corresponding to an invariance under rotation of $2\pi/s$. Hence we write

$$w(x, y) = \sum_{m=0}^{\infty} a_m(x)\cos(ms\rho y); \quad \phi(x, y) = \sum_{m=0}^{\infty} b_m(x)\cos(ms\rho y), \quad s \in \mathbb{N}.$$

Substituting into the von Kármán–Donnell equations and taking the L^2 inner product with $\cos(ms\rho y)$, we obtain a system of nonlinear ODEs for the Fourier modes a_m and b_m for $m = 0, \ldots, \infty$. The Galerkin approximation is formed by taking $m = 0, \ldots, M-1$ for some finite M giving a system of $8M$ first-order ordinary differential equations which we may formally write as

$$\begin{aligned} a_m'''' &= G_{1,m}(a_m, a_m', a_m'', a_m''', b_m, b_m', b_m'', b_m'''); \\ b_m'''' &= G_{2,m}(a_m, a_m', a_m'', a_m''', b_m, b_m', b_m'', b_m'''), \end{aligned} \qquad m = 0, 1, 2, \ldots, M-1, \tag{27}$$

where superscripts denote differentiation with respect to x. Further details on the discretization may be found in [38]. The system (27) of fourth-order ODEs is then similar in nature to the single ODE (1), although more complicated. For the system (27) there are two natural symmetries in x both of which are observed experimentally in the cylinder. In fact, Equation (27) is reversible about each of these symmetries and this can be exploited in the computations. One form of symmetry, termed *cross-symmetric*, is even in even Fourier modes and odd in odd modes. The *symmetric* form is a straightforward symmetry in which all Fourier modes are even. In [8] preliminary results were presented on the cylinder for a *cross symmetric* solution with $s = 11$. The characteristic snaking bifurcation diagram, similar to Figure 7 for the asymmetric case f_1, was found and cellular buckling of the cylinder was observed.

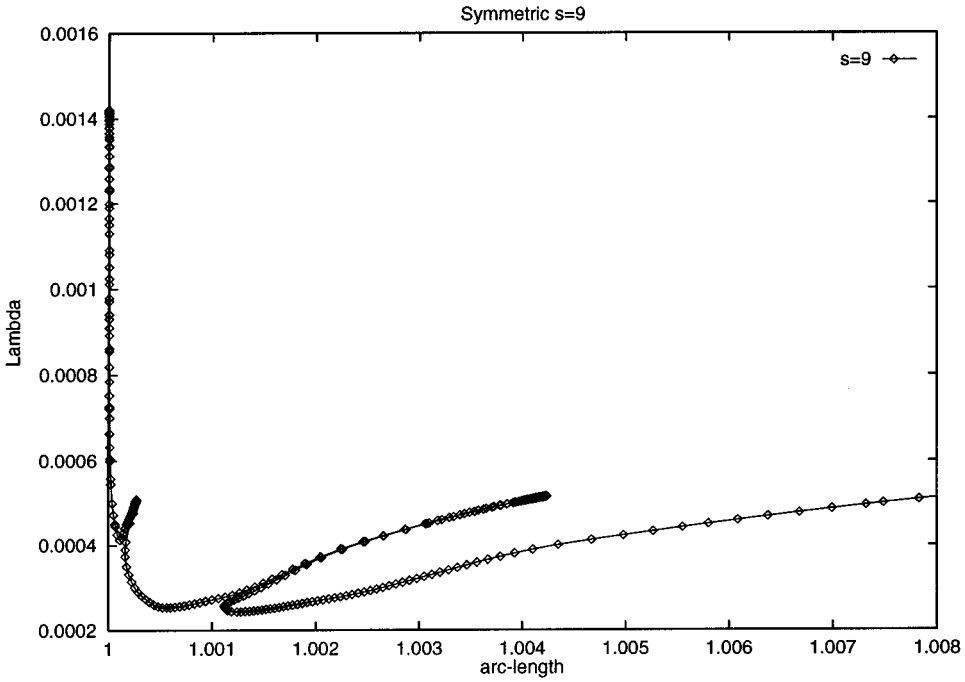

Figure 21. Bifurcation diagram showing end-shortening of the cylinder against load λ for $s = 9$ waves circumferentially.

Here we examine the symmetric case, which is similar in nature to the case f_2 discussed in Section 4. Note that, for the cylinder, these two cases exist without the need to change the form of the nonlinearity, illustrating the more complex nature of the ODEs (27).

For details on the numerical solution of the boundary-value problem solved for these computations, see [38] and for errors in the truncation of the length X, see [39].

In Figure 21 we have plotted the load parameter λ against end-shortening (measured by arc-length) for $s = 9$ circumferential waves. Although it appears from the bifurcation diagram that there is one single form of symmetric solutions for the system (27) of ODEs there are in fact two. This is evident from Figure 22 in which we have plotted the Fourier modes a_k and b_k for $k = 0, 1, \ldots, 5$ at $\lambda = 4.5 \times 10^{-4}$ and for arc-length= 1.00306 for two different symmetric solutions. In panel (a) of the figure we see that the odd modes are at a maximum at the symmetric section at $X = 500$ whereas in panel (b) we see that the odd modes are at a minimum at $X = 500$.

In Figure 23a we have reconstructed the displacement and stress function on the cylinder for the Fourier modes shown in Figure 22. Note that the two different symmetries of the ODEs (27) in fact correspond to the same buckled cylinder solution – one is simply a rigid rotation of the other.

Each time a maximum is passed in the snaking bifurcation diagram of Figure 21, an extra 'hump' appears in the solution. In Figure 23b we have plotted the reconstructed the displacement and stress function on the cylinder for the same value of $\lambda = 4.5 \times 10^{-4}$ but at an arc-length of 1.0058022, i.e. after passing through another maximum and picking up a further cellular buckle.

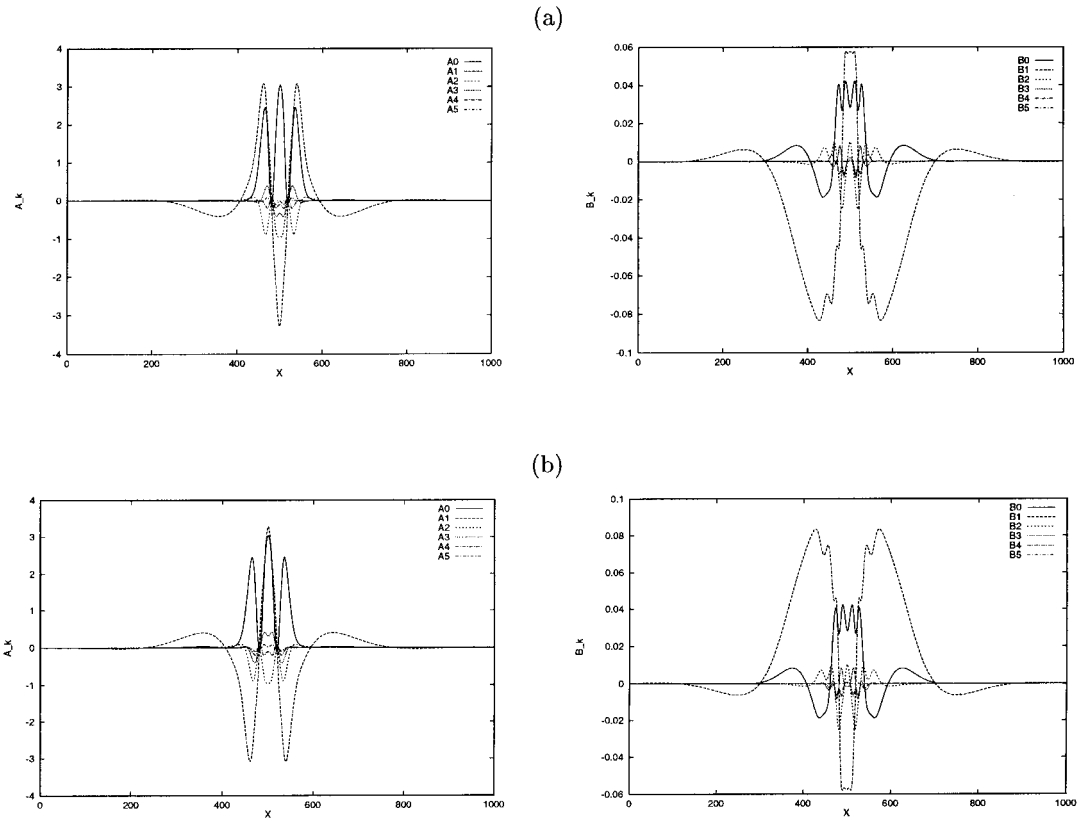

Figure 22. Fourier modes for a_k (left) and b_k (right) as computed from (27) for two different forms of symmetry: (a) odd solutions abut $X = 500$, (b) even solutions about $X = 500$.

Note that the results produced here for the symmetric case and in [8] for the cross-symmetric case are in subspaces corresponding to $s = 9$ and $s = 11$ waves circumferentially. The lower bound of the snaking behaviour observed for the cylinder is of practical interest since, for a given subspace, it gives a lower bound on the Maxwell load and on the load at which the cylinder may be expected to first undergo an unstable response. However, in the full system the situation is far more complicated since solutions will jump from one subspace to another and hence experimentally the snaking bifurcation diagram of Figure 21 is not fully observed.

6. Conclusion

This paper has contained a rag bag of different methods and problems which together appear to point towards a fundamental new explanation of the postbuckling behaviour of structures with destiffening then restiffening characteristics. Some of the details and connectivities between the different strands have not been fleshed out fully, and these are left to future work. However, a coherent picture appears to be emerging, which can be summed up in Figure 19. Under rigid end-displacement, a long structure buckles in a cellular manner between a maximum and minimum load (which are both less than the linear critical load) which bound the oscillating postbuckling curve. If the structure were able to jump to the global minimum solution, then the

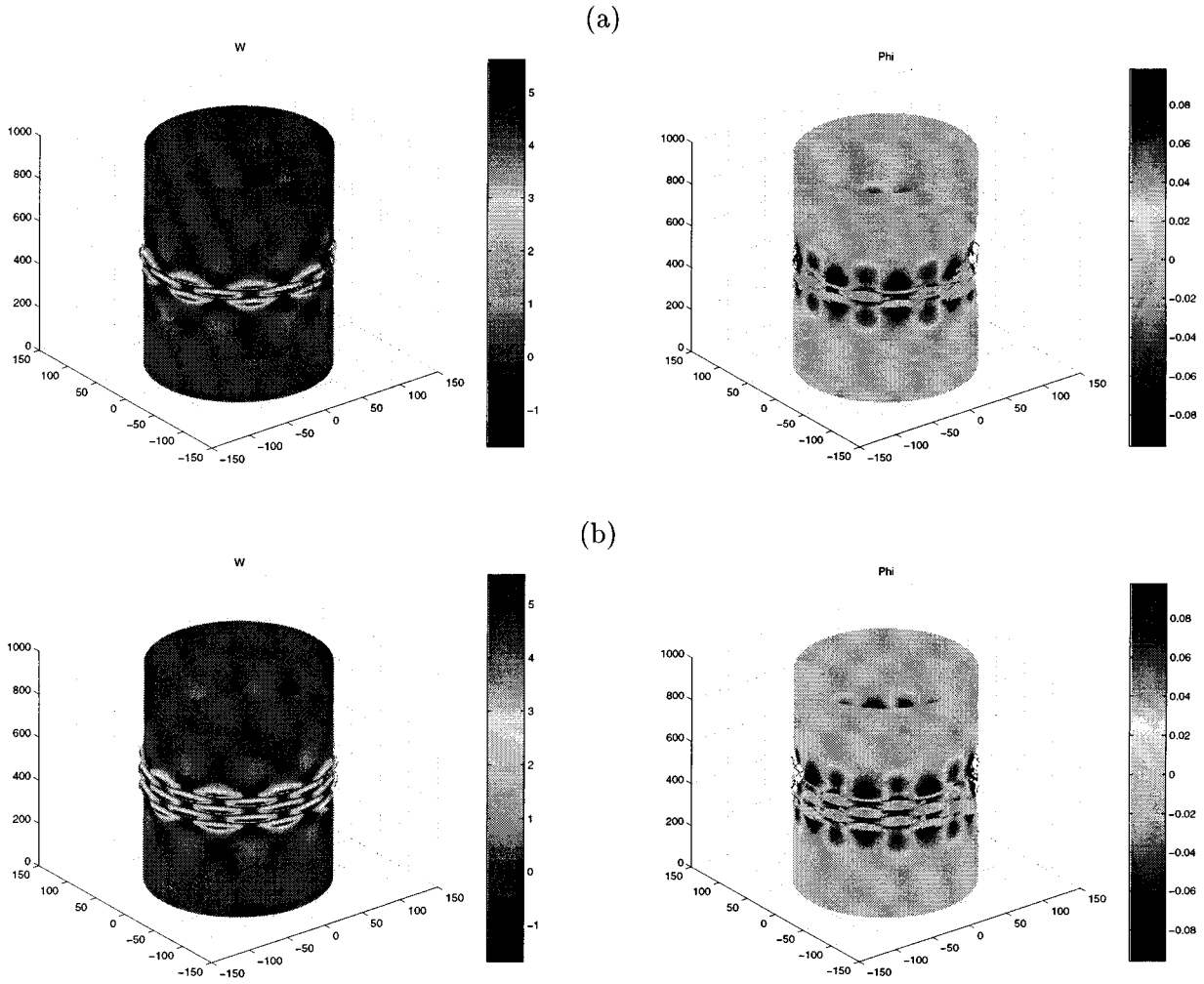

Figure 23. Deflection $w(x, y)$ and stress function $\phi(x, y)$ reconstructed from the numerical solutions on the localized buckling path at $\lambda = 4.5 \times 10^{-4}$. After each pass though a maximum the solution picks up an additional cell.

path for large displacement will become approximately flat at the Maxwell load. Of course, many real structures will not undergo such a sequence due, for example, to plastic necking, other microscopic effects, or (as for the cylinder) a jump into into an entirely different mode of buckling. Nevertheless, we appear to have found a ubiquitous postbuckling scenario, and future work by some of us will illustrate this in yet more physical situations. Examples already known to us include the wrapping up of a torsionally buckled rod constrained to lie inside a cylindrical pipeline, and a model for kink banding in compressed layered materials.

A particularly gratifying feature of this work is that so many different methods – normal form analysis, asymptotics, numerics, physical argument, variational arguments, and a link model caricature – have all played a role in the explanation.

Acknowledgement

The authors are indebted to Boris Buffoni for useful discussions.

References

1. Champneys, A. R., Hunt, G. W., and Thompson, J. M. T. (eds.), *Localization and Solitary Waves in Solid Mechanics*, special issue of *Philosophical Transactions of the Royal Society of London Series A* **355**, 1997, 2073–2213.
2. Lord, G. J., Champneys, A. R., and Hunt, G. W., 'Computation of localized post buckling in long axially-compressed cylindrical shells', *Philosophical Transactions of the Royal Society of London Series A* **355**, 1997, 2137–2150 (special issue on *Localization and Solitary Waves in Solid Mechanics*, A. R. Champneys, G. W. Hunt, and J. M. T. Thompson (eds.).)
3. Thompson, J. M. T. and Champneys, A. R., 'From the helix to localized writhing in the torsional post buckling of elastic rods', *Proceedings of the Royal Society of London Series A* **452**, 1996, 117–138.
4. Goriely, A. and Tabor, M., 'Nonlinear dynamics of filaments III – Instabilities of helical rods', *Proceedings of the Royal Society of London Series A* **453**, 1997, 2583–2601.
5. Mielke, A. and Holmes, P., 'Spatially complex equilibria of buckled rods', *Archive Rational Mechanics and Analysis* **101**, 1988, 319–348.
6. Hunt, G. W. and Everall, P. R., 'Arnold tongues and mode jumping in the supercritical post-buckling of an archetypal elastic structure', *Proceedings of the Royal Society of London Series A* **455**, 1999, 125–140.
7. Woods, P. D. and Champneys, A. R., 'Heteroclinic tangles in the unfolding of a degenerate Hamiltonian Hopf bifurcation', *Physica D* **129**, 1999, 147–170.
8. Hunt, G. W., Lord, G. J., and Champneys, A. R., 'Homoclinic and heteroclinic orbits underlying the post-buckling of axially-compressed cylindrical shells', *Computer Methods in Applied Mechanics and Engineering* **170**, 1999, 239–251.
9. Hunt, G. W. and Wadee, M. A., 'Localization and mode interaction in sandwich structures', *Proceedings of the Royal Society of London Series A* **454**, 1998, 1197–1216.
10. Wadee, M. A. and Hunt, G. W., 'Interactively induced localized buckling in sandwich structures with core orthotropy', *ASME, Journal of Applied Mechanics* **65**, 1998, 523–528.
11. Budd, C. J. and Peletier, M. A., 'Self-similar fold evolution under prescribed end-shortening', *SIAM Journal on Applied Mathematics*, 1998, to appear. Preprint 98/08, Department of Mathematical Sciences, University of Bath.
12. Budd, C. J., Hunt, G. W., and Peletier, M. A., 'Approximate self-similarity in models of geological folding', *Journal of Mathematical Geology*, 1998, to appear. Preprint 98/13, Department of Mathematical Sciences, University of Bath.
13. Hilali, M'F., Métens, S., and Dewel, G., 'Pattern selection in the generalised Swift–Hohenberg model', *Physical Review E* **51**, 1995, 2046–2052.
14. Hunt, G. W., Bolt, H. M., and Thompson, J. M. T., 'Structural localization phenomena and the dynamical phase-space analogy', *Proceedings of the Royal Society of London Series A* **425**, 1989, 245–267.

15. Hunt, G. W. and Wadee, M. K., 'Comparative Lagrangian formulations for localized buckling', *Proceedings of the Royal Society of London Series A* **434**, 1991, 485–502.
16. Devaney, R. L., 'Reversible diffeomorphisms and flows', *Transactions of the American Mathematical Society* **218**, 1976, 89–113.
17. Buffoni, B., Champneys, A. R., and Toland, J. F., 'Bifurcation and coalescence of a plethora of homoclinic orbits for a Hamiltonian system', *Journal of Dynamics and Differential Equations* **8**, 1996, 221–281.
18. Elphick, C., Tirapegui, E., Brachet, M., Coullet, P., and Iooss, G., 'A simple global characterisation for normal forms of singular vector fields', *Physica D* **29**, 1987, 95–127.
19. Iooss, G. and Pérouème, M. C., 'Perturbed homoclinic solutions in reversible 1:1 resonance vector fields', *Journal of Differential Equations* **102**, 1993, 62–88.
20. Dias, F. and Iooss, G., 'Capillary-gravity interfacial waves in infinite depth', *European Journal of Mechanics B – Fluids* **15**, 1996, 367–393.
21. Buffoni, B. and Séré, E., 'A global condition for quasi-random behaviour in a class of conservative systems', *Communications on Pure and Applied Mathematics* **49**, 1996, 285–305.
22. Devaney, R. L., 'Homoclinic orbits in Hamiltonian systems', *Journal of Differential Equations* **21**, 1976, 431–438.
23. Doedel, E. J., Champneys, A. R., Fairgrieve, T. F., Kuznetsov, Y. A., Sandstede, B., and Wang, X.-J., 'AUTO97: Continuation and bifurcation software for ordinary differential equations', 1997. (Available by anonymous FTP from `ftp.concordia.ca` in `/pub/doedel/auto`.)
24. Hofer, H. and Toland, J. F., 'On the existence of homoclinic, heteroclinic, and periodic orbits for a class of indefinite Hamiltonian systems', *Mathematische Annalen* **268**, 1984, 387–403.
25. Peletier, L. A. and Troy, W. C., 'A topological shooting method and the existence of kinks of the Extended Fisher–Kolmogorov equation', *Topological Methods in Nonlinear Analysis* **6**, 1996, 331–355.
26. Kalies, W. D. and Vandervorst, R. A. C. M., 'Multitransition homoclinic and heteroclinic solutions of the extended Fisher–Kolmogorov equation', *Journal of Differential Equations* **131**, 1996, 209–228.
27. van den Berg, J. B., 'Uniqueness of solutions for the Extended Fisher–Kolmogorov equation', *Comptes Rendus de L'Académie des Sciences Série I* **326**, 1998, 447–452.
28. Gibson, L. J. and Ashby, M. F., 'The mechanics of three-dimensional cellular materials', *Proceedings of the Royal Society of London Series A* **382**(1782), 1982, 43–59.
29. Gibson, L. J., Ashby, M. F., Schjaer, G. S., and Robertson, C. I., 'The mechanics of two-dimensional cellular materials', *Proceedings of the Royal Society of London Series A* **382**(1782), 1982, 25–42.
30. Price, N. J. and Cosgrove, J. W., *Analysis of Geological Structures*, Cambridge University Press, Cambridge, 1990.
31. Johnson, A. M. and Fletcher, R. C., *Folding of Viscous Layers*, Columbia University Press, New York, 1994.
32. Hunt, G. W., Wadee, M. K., and Shiacolas, N., 'Localized elasticae for the strut on the linear foundation', *ASME, Journal of Applied Mechanics* **60**, 1993, 1033–1038.
33. Zeeman, E. C., *Catastrophe Theory: Selected Papers, 1972–1977*, Addison-Wesley, Reading, MA, 1977.
34. Hunt, G. W. and Lucena Neto, E., 'Maxwell critical loads for axially-loaded cylindrical shells', *ASME, Journal of Applied Mechanics* **60**(3), 1993, 702–706.
35. Thompson, J. M. T. and Hunt, G. W., *A General Theory of Elastic Stability*, Wiley, London, 1973.
36. Koiter, W. T., 'On the stability of elastic equilibrium', Ph.D. Thesis, University of Delft, 1945. English Translation: Technical Report AFFDL-TR-70-25 Air Force Flight Dynamics Laboratory, 1970.
37. Yamaki, N., *Elastic Stability of Circular Cylindrical Shells*, Applied Mathematics and Mechanics, Vol. 27, Elsevier, Amsterdam, 1984.
38. Lord, G. J., Champneys, A. R., and Hunt, G. W., 'Computation of homoclinic orbits in partial differential equations: An application to cylindrical shell buckling', *SIAM Journal on Scientific Computing*, 1998, to appear.
39. Lord, G. J., Peterhof, D., Sandstede, B., and Scheel, A., 'Numerical computaton of solitary waves in semilinear elliptic problems on infinite cylinders', *SIAM Journal on Numerical Analysis*, 1998, submitted.